

Pressure-induced Co^{2+} photoluminescence quenching in MgAl_2O_4

Lucie Nataf* and Fernando Rodríguez†

MALTA Consolider Team, DCITIMAC, Faculty of Science, University of Cantabria, 39005 Santander, Spain

Rafael Valiente

MALTA Consolider Team, Department of Applied Physics, University of Cantabria, 39005 Santander, Spain

(Received 12 July 2012; published 17 September 2012)

This work investigates the electronic structure and photoluminescence (PL) of Co^{2+} -doped MgAl_2O_4 and their pressure dependence by time-resolved spectroscopy. The variations of the visible absorption band and its associated emission at 663 nm ($\tau = 130$ ns at ambient conditions) with pressure/temperature can be explained on the basis of a configurational energy model. It provides an interpretation for both the electronic structure and the excited-state phenomena yielding photoluminescence emission and the subsequent quenching. We show that there is an excited-state crossover (ESCO) [${}^4T_1(P) \leftrightarrow {}^2E(G)$] at ambient pressure, which is responsible for the evolution of the emission spectrum from a broadband emission between 300 K and 100 K to a narrow-line emission at lower temperatures. Contrary to expectations from the Tanabe-Sugano diagram, instead of enhancing ESCO phenomena, pressure reduces PL and even suppresses it (PL quenching) above 6 GPa. We explain such variations in terms of pressure-induced nonradiative relaxation to lower excited states: ${}^2E(G) \rightarrow {}^4T_1(F)$. The variation of PL intensity and its associated lifetime with pressure supports the proposed interpretation.

DOI: [10.1103/PhysRevB.86.125123](https://doi.org/10.1103/PhysRevB.86.125123)

PACS number(s): 71.70.Ch, 78.47.da, 78.55.Hx, 81.40.Vw

I. INTRODUCTION

The optical and structural properties of $\text{MgAl}_2\text{O}_4:\text{Co}^{2+}$ have received considerable attention due to its capabilities as Q -switch and nonlinear optics material,^{1–4} its potential tunability for upconversion photoluminescence (PL) in bulk⁴ and nanoparticles,⁵ and the lack of pressure shifts of the dominant ${}^4A_2(F) \rightarrow {}^4T_1(P)$ crystal-field-dependent absorption band due to covalency effects.^{6–8} All these characteristics together with the fourfold tetrahedral coordination of Co^{2+} (T_d) make the present system a model for different Co^{2+} -incorporating oxides like blue pigments (CoAl_2O_4) (Refs. 9 and 10), optoelectronics and spintronics ($\text{ZnO}:\text{Co}^{2+}$) (Refs. 11–13), or phosphors ($\text{ZnAl}_2\text{O}_4:\text{Co}^{2+}$) (Refs. 6 and 14).

$\text{MgAl}_2\text{O}_4:\text{Co}^{2+}$ crystallizes in the spinel structure (cubic $Fd\bar{3}m$, $a = 8.070$ Å) (Ref. 15) where Co^{2+} impurities substitute Mg^{2+} at the T_d Mg site ($R_{\text{Mg-O}} = 1.918$ Å). The electronic structure of Co^{2+} (T_d) in $\text{MgAl}_2\text{O}_4:\text{Co}^{2+}$ makes it attractive for investigating nonlinear optics and PL phenomena. In particular, we are interested in elucidating whether modifications of the crystal-field strength on Co^{2+} can induce excited-state crossover (ESCO) yielding PL changes from ${}^4T_1(P) \rightarrow {}^4A_2(F)$ broadband emission to ${}^2E(G) \rightarrow {}^4A_2(F)$ rubylike line emission. This transformation will potentially enhance the PL capability of tetrahedral $\text{Co}^{2+}(3d^7)$ systems as efficient PL materials. Besides, there are fundamental aspects associated with the excited-state dynamics leading to $\text{Co}^{2+}(T_d)$ -related PL which deserve clarification.^{11,12,16,17}

At ambient conditions the $\text{MgAl}_2\text{O}_4:\text{Co}^{2+}$ PL consists of three broadband emissions peaking at 1.88, 1.41, and 0.98 eV (660, 880, and 1270 nm, respectively),^{1,9,11,16} which are associated with electronic transitions from the ${}^4T_1(P)$ excited state to the ${}^4A_2(F)$ ground state and the low-lying excited states, ${}^4T_2(F)$ and ${}^4T_1(F)$, respectively. This is shown schematically in the Tanabe-Sugano diagram of Fig. 1 (Refs. 9 and 18). Nevertheless, the visible PL at 1.88 eV evolves with

temperature from a broadband emission (300 K to 100 K) to a narrow-line emission located at 1.931 eV (642.0 nm) at 6 K (Fig. 2). A similar low-temperature emission was also observed in the isostructural $\text{ZnAl}_2\text{O}_4:\text{Co}^{2+}$ (Ref. 6) whose peak located at 1.950 eV (636 nm) was ascribed to the ${}^2E(G) \rightarrow {}^4A_2(F)$ electronic transition. This peak, which is the dominant one in the emission spectrum at low temperature, indicates that the ${}^2E(G)$ configurational energy minimum at ambient pressure lies below the ${}^4T_1(P)$ minimum. Although ${}^4T_1(P)$ appears well above ${}^2E(G)$ in the Tanabe-Sugano diagram at the crystal field of $\text{MgAl}_2\text{O}_4:\text{Co}^{2+}$ (Fig. 1), the energy minima of these states are very close due to the higher electron-lattice coupling interaction of the ${}^4T_1(P)$ state with respect to the spin-flip-like ${}^2E(G)$ state. This causes the minimum of the ${}^4T_1(P)$ potential energy parabola to be displaced with respect to the corresponding parabola minima of the ${}^4A_2(F)$ ground state and the ${}^2E(G)$ excited state, and thus the zero-phonon line (ZPL) energies in $\text{MgAl}_2\text{O}_4:\text{Co}^{2+}$ and $\text{ZnAl}_2\text{O}_4:\text{Co}^{2+}$ must satisfy $E_{\text{ZPL}}[{}^2E(G)] \leq E_{\text{ZPL}}[{}^4T_1(P)]$ or, analogously, $\Delta_{\text{ZPL}} = E_{\text{ZPL}}[{}^4T_1(P)] - E_{\text{ZPL}}[{}^2E(G)] \geq 0$. Although both spinels show similar Co^{2+} PL spectra, the position of the ${}^2E(G)$ ZPL in $\text{MgAl}_2\text{O}_4:\text{Co}^{2+}$ (1.931 eV) appears redshifted by 19 meV with respect to $\text{ZnAl}_2\text{O}_4:\text{Co}^{2+}$ (1.950 eV). As discussed later on, this difference should be mainly ascribed to a slight decrease of the B and C Racah parameters in $\text{MgAl}_2\text{O}_4:\text{Co}^{2+}$ with respect to $\text{ZnAl}_2\text{O}_4:\text{Co}^{2+}$. This reduction is caused by the increase of Co-O bond covalency due to the increase of chemical pressure at the Co^{2+} divalent site upon passing from ZnAl_2O_4 ($a = 8.085$ Å; $R_{\text{Zn-O}} = 1.922$ Å) (Ref. 19) to MgAl_2O_4 ($a = 8.070$ Å; $R_{\text{Mg-O}} = 1.918$ Å) (Ref. 15). Similarly to the pressure-induced redshifts in $\text{Al}_2\text{O}_3:\text{Cr}^{3+}$ (ruby) R lines,²⁰ the nearly crystal-field independent spin-flip ${}^2E(G)$ transition of $\text{Co}^{2+}(T_d)$ shifts to lower energies upon volume reduction. Hence the study of pressure effects on the PL properties of $\text{Co}^{2+}(T_d)$ is better suited in the more chemically compressed $\text{MgAl}_2\text{O}_4:\text{Co}^{2+}$.

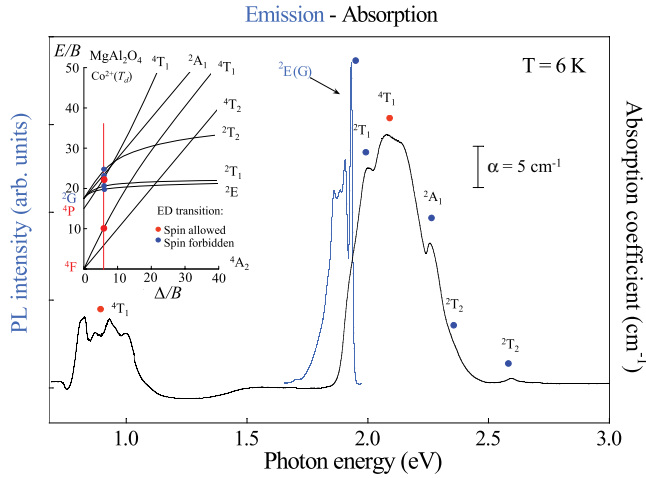


FIG. 1. (Color online) The 6 K absorption and emission spectra of $\text{MgAl}_2\text{O}_4:\text{Co}^{2+}$ single crystal. The peak assignment corresponds to electronic crystal-field transitions from the ${}^4A_2(F)$ ground state of $\text{Co}^{2+}(T_d)$ to the excited state $\Gamma(T_d)$ irreps). The Tanabe-Sugano diagram of $d^7(T_d)$ for $C/B = 4.5$ is included. The experimental crystal-field energies obtained from the optical spectra are represented by spots at the fit point $\Delta/B = 5.3$. Fitting parameters are $B = 0.098$ eV (790 cm^{-1}) and $\Delta_{CF} = 0.52$ eV (4200 cm^{-1}).

Hereto we investigate the spectral features and PL phenomena associated with the ${}^4T_1(P) \leftrightarrow {}^2E(G)$ ESCO and

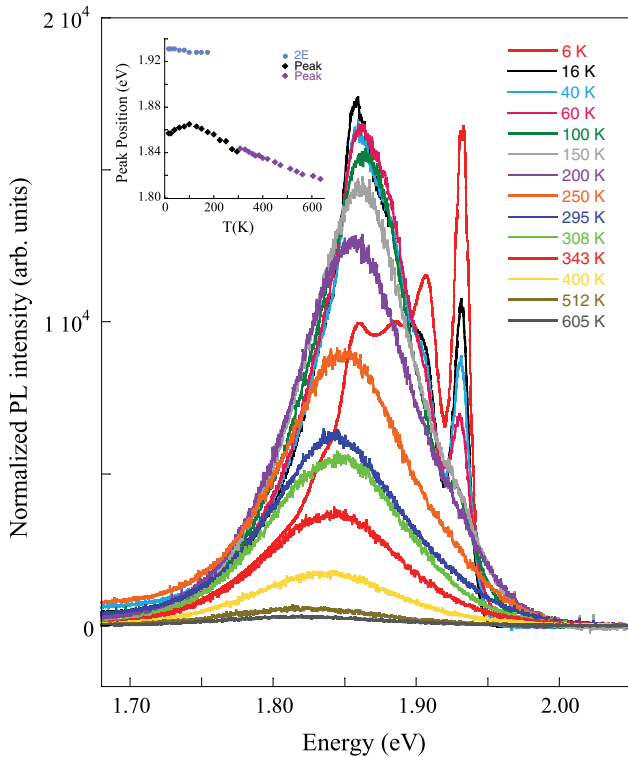


FIG. 2. (Color online) Temperature evolution of the time-resolved emission spectra of $\text{MgAl}_2\text{O}_4:\text{Co}^{2+}$. Each spectrum was taken 30 ns after pulsed laser excitation at 530 nm using a counting gate of $10\ \mu\text{s}$. The inset shows the temperature evolution of the band centroid corresponding to the ${}^2E(G) + {}^4T_1(P) \rightarrow {}^4A_2(F)$ emissions and the ZPL ${}^2E(G) \rightarrow {}^4A_2(F)$.

whether a transformation from a broadband PL emission to a narrow-line emission can be eventually induced by pressure at room temperature ($\Delta_{ZPL} \gg 300k_B$), or whether nonradiative channels are activated. Our aim is to find structural requirements for $\text{Co}^{2+}(T_d)$ to be followed for improving the PL quantum yield of $\text{Co}^{2+}(T_d)$ -based oxides. Contrary to other sharp-line PL associated with the ${}^2E(G) \rightarrow {}^4A_2(F)$ transition like Cr^{3+} in Al_2O_3 (ruby)²⁰ or $\text{LiCaAlF}_6:\text{Cr}^{3+}$ (Ref. 21), $\text{Co}^{2+}(T_d)$ involves symmetry- and spin-allowed electric-dipole transitions, thus providing a more efficient pumping for PL.

II. EXPERIMENT

Single crystals of $\text{MgAl}_2\text{O}_4:\text{Co}^{2+}$ (0.25 mol%) were grown as described elsewhere.¹⁷ Unavoidable Cr^{3+} traces were detected through the characteristic $\text{Cr}^{3+}(O_h)$ sharp-line PL around 1.805 eV (687 nm).^{17,22,23} From absorption measurements we estimated the Cr^{3+} concentration to be smaller than 10 ppm.

The absorption spectra, under ambient conditions and at low temperature, were obtained on a Cary 6000i (Varian). The 6 K emission spectrum was obtained using a cw Kr^+ laser (Coherent Innova I-300) and a double monochromator (Jobin-Yvon, Ramanor U1000). An Oxford Microstat liquid-helium-cooled cryostat was employed for high-resolution spectroscopy in the 6 K to 200 K range, and a Scientific Instruments 202 closed-cycle cryostat and an APD-K controller were employed for temperature dependence studies in the 15 K to 300 K range. High-temperature measurements in the 300 K to 800 K range were performed with a Leitz 350 heating stage.

Time-resolved emission and excitation spectra were obtained using a Vibrant B 355 II OPO tunable laser as the excitation source. The OPO laser beam was focused backward on the sample with a $20\times$ microscope objective, and the PL was collected upward with another $20\times$ objective and a Horiba-Jobin-Yvon fast-intensified charge-coupled device (iCCD) with 5-ns time resolution. The excitation spectra were corrected from the pulsed energy using a beam splitter together with a powermeter. For the lifetime measurements, the PL decay signal was recorded with the iCCD.

Hydrostatic pressure experiments in the 0–6 GPa range were carried out on a membrane-type diamond anvil cell (MDAC). Inconel gaskets (200 μm in thickness) were preindented and suitable 200- μm -diameter holes were perforated with a Betsa motorized electrical discharge machine. The MDAC was loaded with a suitable single crystal and ruby microspheres ($<10\ \mu\text{m}$ in diameter) using a methanol-ethanol-water mixture (16:3:1) as the pressure transmitting medium. Due to partial decomposition and graphitization of the transmitting medium induced by pulsed laser focusing, we also carried out high-pressure experiments using nitrogen as the pressure transmitting medium. In all cases experiments were performed in the hydrostatic regime and the pressure was calibrated from the ruby PL.^{20,24}

III. RESULTS AND DISCUSSION

A. Optical absorption spectra and photoluminescence of $\text{MgAl}_2\text{O}_4:\text{Co}^{2+}$

The MgAl_2O_4 spinel structure ($Fd\bar{3}m$) is stable up to 65 GPa (Ref. 25) at room temperature. The 6 K absorption

spectrum of the $\text{MgAl}_2\text{O}_4:\text{Co}^{2+}$ single crystal and the corresponding emission spectrum after 530-nm excitation are shown in Fig. 1 together with the $\text{Co}^{2+}(d^7;T_d)$ Tanabe-Sugano diagram. The main features of the absorption spectrum are associated with the spin-allowed transitions from the ${}^4A_2(F)$ ground state to the ${}^4T_1(F)$ state at 0.9 eV and the ${}^4T_1(P)$ state at 2.1 eV. Spin-forbidden transitions from ${}^4A_2(F)$ to spin doublets arising from the 2G multiplet (2E , 2T_1 , 2A_1 , 2T_2 in order of increasing energy) and 2H multiplet (2T_2) can be identified despite their low intensity.^{1,6,16,17} Their transition energy can be accounted for on the basis of the semiempirical Tanabe-Sugano formalism¹⁸ using Racah parameters, $B = 98$ meV and $C = 440$ meV, and crystal-field splitting, $\Delta_{\text{CF}} = 0.52$ eV (Table I). While B and C are similar to other T_d and O_h Co^{2+} oxides,⁹ the crystal-field strength in T_d is half the crystal-field strength in O_h : $\Delta_{\text{CF}}(O_h) = 0.90$ eV for Co_2SiO_4 or 1.15 eV for $\text{MgO}:\text{Co}^{2+}$ (Ref. 9). Besides the crystal-field theory estimates,^{9,26} this behavior reflects a general trend about the crystal-field splitting observed in transition-metal ions with 4- T_d and 6- O_h coordinations beyond the particular crystal structure of the host crystal. $\Delta_{\text{CF}}(O_h) \approx 2 \times \Delta_{\text{CF}}(T_d)$ irrespective of the ligand being O, Cl, or Br (Refs. 9, 26, and 27). As far as we know there is no example of tetrahedrally coordinated Co^{2+} in fluorides.

Previous studies on $\text{MgAl}_2\text{O}_4:\text{Co}^{2+}$ (Refs. 1, 5, 16, 17, and 28–30) show that the PL consists of three emission bands at 1.88, 1.41, and 0.98 eV, which are assigned to the ${}^4T_1(P) \rightarrow {}^4A_2(F)$, ${}^4T_1(P) \rightarrow {}^4T_2(F)$, and ${}^4T_1(P) \rightarrow {}^4T_2(F)$ transitions, respectively. In this study, we focus on the visible emission ${}^4T_1(P) \rightarrow {}^4A_2(F)$ since new features associated with ESCO can be induced by temperature or pressure. The 6 K emission spectrum shows a narrow peak structure, characteristic of the ${}^2E(G) \rightarrow {}^4A_2(F)$ spin-flip transition rather than the ${}^4T_1(P) \rightarrow {}^4A_2(F)$ broadband emission. This assignment is supported by the huge difference between emission lifetime values measured at low temperature (3 μs) compared to room temperature (130 ns). Besides nonradiative processes, this difference clearly indicates that the low-temperature emitting state involves a Co^{2+} spin-forbidden transition in T_d . The most intense peak at 1.931 eV is the ZPL of the mainly ${}^2E(G)$ state, whereas the fine structure at lower energy corresponds to its vibronic sideband. It is worth noting that the phonon sideband does not reflect the vibrational density of states of the host crystal following infrared reflection spectroscopy measurements and *ab initio* calculations in MgAl_2O_4 (Ref. 31). By contrast, the phonon sideband is mainly associated with electron-vibrational coupling to local Co-O modes of 26 meV (210 cm^{-1}) as is evidenced by the regular separation of the observed peaks at 1.931 (ZPL), 1.905, 1.879, and 1.834 eV. By comparing this local mode with MgAl_2O_4 phonons, the coupled local mode has a vibrational energy slightly lower than that of the TO_1 and LO_1 phonons of 28 meV (227 cm^{-1}) thus pointing out the softening of the vibrational local mode when Co^{2+} replaces Mg^{2+} in the host lattice. This phonon sideband is missed in absorption since the ${}^4A_2(F) \rightarrow {}^2E(G)$ transition is observed as a shoulder in the main absorption band, which consists of different components: ${}^2E(G)$ at 1.93 eV, ${}^2T_1(G)$ at 2.00 eV, ${}^4T_1(P)$ at 2.10 eV, ${}^2A_1(G)$ at 2.25 eV, and ${}^2T_2(G)$ at 2.34 eV (Table I). With the exception of ${}^4T_1(P)$, all components correspond to spin-

TABLE I. Experimental transition energy taken from the optical absorption and emission spectra of $\text{MgAl}_2\text{O}_4:\text{Co}^{2+}$ at $T = 6$ K (Figs. 1 and 2), and calculated energies for Co^{2+} in T_d symmetry. The calculated energies were obtained by fitting the experimental energies to the energy terms of a d^7 electron configuration.¹⁸ The fit Racah parameters, B and C , and the crystal-field splitting, Δ_{CF} , are collected together with the standard deviation, σ .

Absorption peak assignment for $\text{Co}^{2+}(T_d)$	$\text{MgAl}_2\text{O}_4:\text{Co}^{2+}$		$T = 6$ K	
	Observed (eV)	Calculated (eV)	Observed (cm^{-1})	Calculated (cm^{-1})
${}^4A_2(F) \rightarrow {}^4T_2(F)$		0.52		4100
$\rightarrow {}^4T_1(F)$	0.9	0.89	7200	7200
$\rightarrow {}^2E(G)$	1.931	1.931	15 575	15 575
$\rightarrow {}^2T_1(G)$	2.00	2.00	16 100	16 100
$\rightarrow {}^4T_1(P)$	2.10	2.13	16 900	17 200
$\rightarrow {}^2A_1(G)$	2.25	2.23	18 150	18 000
$\rightarrow {}^2T_2(G)$	2.34 (sh)	2.33	18 900	18 800
$\rightarrow {}^2T_2(H)$	2.60	2.60	21 000	21 000
B		0.098		790
C		0.440		3550
C/B		4.5		4.5
Δ_{CF}		0.52		4200
Δ_{CF}/B		5.3		5.3
σ		0.014		120

forbidden transitions whose intensity appears enhanced due to spin-orbit coupling with ${}^4T_1(P)$ (Fano resonance, Fig. 1). A similar effect has been observed in 6-coordinated $\text{Cr}^{3+}(O_h)$ in fluorides³² and oxides^{33,34} where the first absorption shows a triplet structure associated with the mixing of the ${}^4T_2(F)$, ${}^2E(G)$, and ${}^2T_1(G)$ excited states by the spin-orbit interaction.²¹ The main difference between 4-coordinated $\text{Co}^{2+}(T_d)$ and 6-coordinated $\text{Cr}^{3+}(O_h)$ in oxides is the Δ/B ratio. It is only of 5.3 for Co^{2+} in MgAl_2O_4 whereas it is of 23 for Cr^{3+} in $\text{Gd}_3\text{Ga}_5\text{O}_{12}$ due to the big difference between the crystal-field energy of each ion.^{33,34} Nevertheless, both systems are located near an excited-state crossover point of the Tanabe-Sugano diagram (Fig. 1) and, therefore, optical absorption bands associated with spin-forbidden transitions of crossing states appear to be enhanced by the spin-orbit interaction between ${}^4T_1(P)$ and ${}^2E(G)$ and ${}^2T_2(G)$ excited states.

B. Temperature study

1. Temperature dependence

Regarding the temperature evolution of the emission spectra from 6 K up to 600 K, shown in Fig. 2, one can deduce that the emission actually comes from two electronic states: ${}^4T_1(P)$ and ${}^2E(G)$, the ${}^2E(G)$ state being slightly below the ${}^4T_1(P)$ state. At low temperatures the emission from the ${}^2E(G)$ state dominates the PL spectrum. Its evolution from a narrow-line structure at low temperature to a broadband emission at high temperature is due to the progressive population of the ${}^4T_1(P)$ state at the expense of the ${}^2E(G)$ state with increasing temperature according to the Boltzmann distribution. However, this behavior contrasts with the evolution of the absorption spectrum (Fig. 3). Apart from thermal broadening of the different components forming

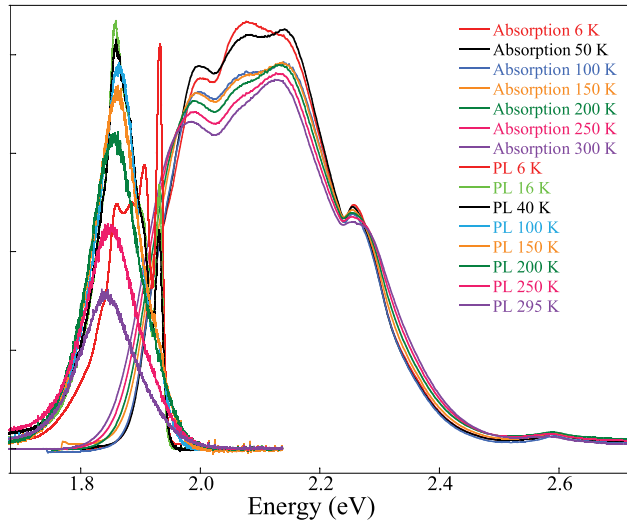


FIG. 3. (Color online) Variation of the optical absorption and emission spectra of $\text{MgAl}_2\text{O}_4:\text{Co}^{2+}$ with temperature in the 6 K to 300 K range at ambient pressure. Note the slight temperature dependence of the absorption spectra in contrast to the drastic change of the emission. The time-resolved emission spectra were obtained upon pulsed laser excitation at 565 nm and the intensity was normalized taking into account instrumental response and the PL quantum yield (see text).

the broad absorption band, no significant effect is observed upon varying temperature. In Fig. 3 the emission spectra have been normalized to the pumping power. The PL quantum yield, defined as $\eta(T) = \frac{\tau_{\text{rad}}^{-1}}{\tau_{\text{rad}}^{-1} + \tau_{\text{nr}}^{-1}}$, has been derived from lifetime measurements as a function of temperature. Here τ_{rad}^{-1} and τ_{nr}^{-1}

means the transition probability associated with the radiative transition from ${}^4T_1(P)$ and ${}^2E(G)$ states in thermal equilibrium at a given temperature and the total transition probability, including nonradiative deexcitation processes, respectively. The measured transition probability through the time-dependent PL decay $I(t)$ is thus given by $\tau^{-1} = \tau_{\text{rad}}^{-1} + \tau_{\text{nr}}^{-1}$, with τ_{nr}^{-1} being the nonradiative contribution. It has to be mentioned that the 6 K high-resolution emission spectrum was obtained under cw excitation with the 520.8-nm line of a Kr^+ laser and a double monochromator providing a spectral resolution of 0.5 cm^{-1} . The temperature dependence of the emission spectra and the associated lifetime was obtained under pulsed excitation and an intensified fast iCCD (see Experiment). Figure 4 shows the temperature dependence of the PL lifetime in the 6 K to 600 K range. The variation of $\tau(T)$ clearly reflects, first, the change of population between the short-lived ${}^4T_1(P)$ and the long-lived ${}^2E(G)$ states in the low-temperature range (6 K to 200 K) as shown in the inset and, second, the thermally activated nonradiative deexcitation processes in the high-temperature range (300 K to 600 K). It must be noted that the different plot ordinates, τ or τ^{-1} , selected in each temperature interval provide accurate descriptions of the radiative (τ_{rad}^{-1}) and nonradiative (τ_{nr}^{-1}) processes in terms of the corresponding transition probabilities. This representation allows us to derive the PL quantum yield as a function of temperature as shown in Fig. 4 (right).

The PL spectra and associated lifetime and their evolution with temperature can be described in terms of a competition between the two ${}^4T_1(P)$ and ${}^2E(G)$ excited states. The deexcitation processes must take into account this competition as well as the thermally activated nonradiative processes. The two emitting states has distinct equilibrium geometry, due to

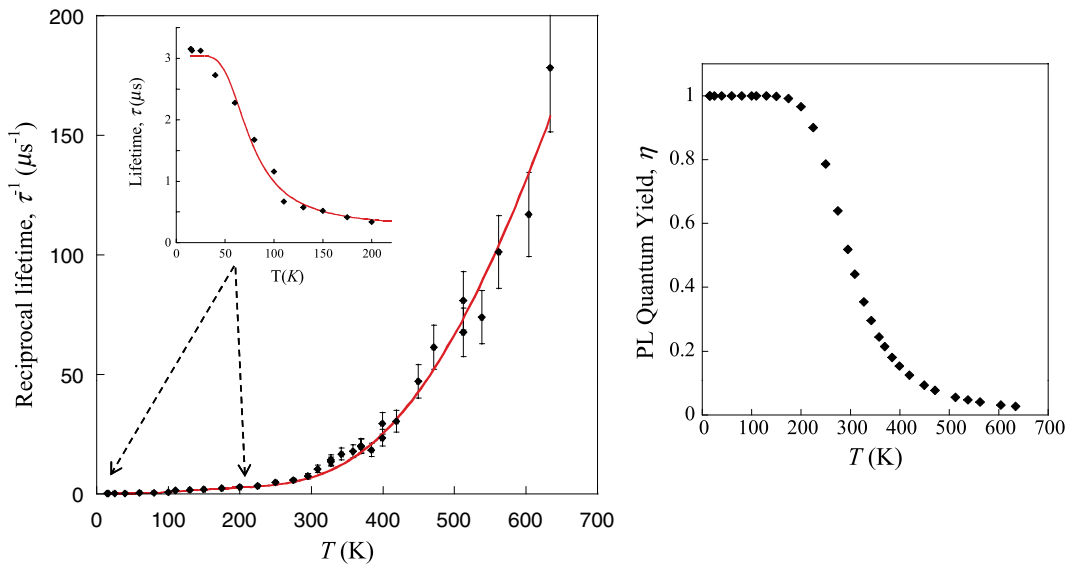


FIG. 4. (Color online) (Left) Variation of the reciprocal of the PL lifetime with temperature in the 6 K to 700 K range of $\text{MgAl}_2\text{O}_4:\text{Co}^{2+}$ using pulsed laser excitation at 530 nm. The inset shows the variation of the PL lifetime in the low-temperature 6 K to 200 K range. Solid lines in both plots represent least-square fits to Eq. (4) with the following fitting parameters: $w_1 = (0.33 \pm 0.01) \times 10^6 \text{ s}^{-1}$; $w_2 = (6.5 \pm 1.4) \times 10^6 \text{ s}^{-1}$; $\Delta_{\text{ZPL}} = (27 \pm 2) \text{ meV}$; $w_1^{\text{nr}} = (2.25 \pm 0.16) \times 10^{10} \text{ s}^{-1}$; and $\Delta_{\text{act}} = (200 \pm 8) \text{ meV}$ at ambient pressure. Note that the choice of $\tau(T)$ or $\tau^{-1}(T)$ for the fitting depends on the sensitivity of the former to changes of thermal populations of ${}^2E(G)$ and ${}^4T_1(P)$ and of the latter to the nonradiative probability. (Right) Variation of PL quantum yield, $\eta(T) = \frac{\tau_{\text{rad}}^{-1}}{\tau_{\text{rad}}^{-1} + \tau_{\text{nr}}^{-1}}$, with temperature as deduced from Eq. (3) using the obtained fit parameters.

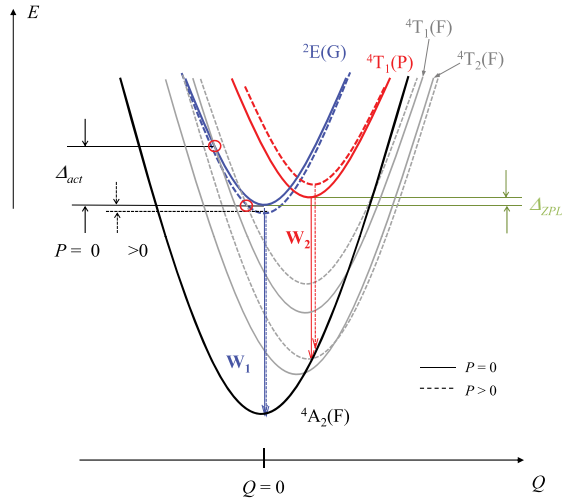


FIG. 5. (Color online) Single-coordinate configurational diagram, $E(Q)$, corresponding to Co²⁺ electronic states involved in the absorption and emission processes in MgAl₂O₄:Co²⁺. Solid lines refer to ambient pressure ($P = 0$) and dotted lines refer to higher pressure ($P > 0$). Δ_{ZPL} and Δ_{act} represent the ZPL energy difference between ${}^2E(G)$ and ${}^4T_1(P)$ and the activation energy for the ${}^2E(G) \rightarrow {}^4T_1(F)$ crossing point yielding nonradiative deexcitation, respectively. The red and blue arrows correspond to the broadband and narrow peak emissions, respectively, shown in Fig. 2.

the different electron-phonon coupling of each state (Fig. 5). Although the ${}^4T_1(P)$ energy in absorption is located at 2.10 eV; i.e., 0.17 eV above ${}^2E(G)$ according to the Tanabe-Sugano diagram (Fig. 1 and Table I), the energies of the minima of the two states are close in the configurational energy curve. Hence, at low temperature, we would expect emission either from 2E or from 4T_1 , if $\Delta_{ZPL} = E({}^4T_1) - E({}^2E)$ is positive or negative, respectively. Depending on the $\Delta_{ZPL}/k_B T$ value, the thermal population of 2E and 4T_1 is given by

$$\begin{aligned} N({}^2E) &= \frac{g({}^2E)}{g({}^2E) + g({}^4T) \times e^{-\Delta_{ZPL}/k_B T}} \\ N({}^4T_1) &= \frac{g({}^4T) \times e^{-\Delta_{ZPL}/k_B T}}{g({}^2E) + g({}^4T) \times e^{-\Delta_{ZPL}/k_B T}}, \end{aligned} \quad (1)$$

with $g({}^2E) = 4$ and $g({}^4T) = 12$ being the total degeneracies of the ${}^2E(G)$ and ${}^4T_1(P)$ states. The changes observed in the visible emission spectrum in the 6 K to 200 K range are due to the different characters of the 2E and 4T_1 states and the small separation of the corresponding ZPL. From the lifetime variation fitting, $\tau(T)$, we obtain $\Delta_{ZPL} = 27$ meV with associated radiative lifetimes of 3.0 μ s and 153 ns for 2E and 4T_1 , respectively (Fig. 4). Therefore, the lifetime decrease with temperature relates to an increase of the transition oscillator strength upon passing from the spin-forbidden ${}^2E(G) \rightarrow {}^4A_2(F)$ (long lifetime) to the spin-allowed ${}^4T_1(P) \rightarrow {}^4A_2(F)$ (short lifetime).

It is worth mentioning that apart from the relative population change $N({}^2E)/N({}^4T_1)$, the further decrease of $\tau(T)$ with temperature above 300 K clearly reveals activation of nonradiative deexcitation processes (Fig. 4). The phenomenological description of $\tau(T)$ following the excited-state dynamics is discussed in the next section.

2. Excited-state crossover: Dynamical model

The PL lifetime of MgAl₂O₄:Co²⁺ ($\tau = 130$ ns) slightly depends on Co²⁺ concentration at ambient conditions. Moreover, the time-dependent PL decay, $I(t)$, measured under pulsed excitation deviates from single exponential behavior as has been previously described.³⁰ The energy-transfer between Co²⁺ was mainly responsible for such nonexponential behavior. Whereas the intensity decay curves can be accurately described by two exponentials, the associated lifetime depends on the radiative and energy-transfer probabilities. Anyway the temporal evolution of the excited-state has been characterized by the averaged lifetime derived from the intensity decay through the following expression:

$$\tau(T) = \frac{\int_0^\infty t I(t) dt}{\int_0^\infty I(t) dt}. \quad (2)$$

The experimental $\tau(T)$ data collected in Fig. 4 were obtained in this way. The thermal dependence of $\tau(T)$ in the 6 K to 600 K range was fitted to the general equation $\tau^{-1} = \tau_{rad}^{-1} + \tau_{nr}^{-1} = w^{rad} + w^{nr}$, where the total deexcitation transition probability is expressed as a sum of the radiative (w^{rad}) and nonradiative (w^{nr}) probabilities. The former term is based on the existence of two emitting states, ${}^2E(G)$ and ${}^4T_1(P)$, in thermal equilibrium, whereas the nonradiative term is expressed by a thermally activated process with an associated energy, Δ_{act} . Thus, the transition probabilities can be written as

$$\begin{aligned} \tau_{rad}^{-1} = w^{rad} &= \frac{w_1 + 3w_2 e^{(-\frac{\Delta_{ZPL}}{kT})}}{1 + 3e^{(-\frac{\Delta_{ZPL}}{kT})}} \\ \tau_{nr}^{-1} = w^{nr} &= \frac{w_1^{nr} e^{-\Delta_{act}/kT}}{1 + 3e^{(-\frac{\Delta_{ZPL}}{kT})}}, \end{aligned} \quad (3)$$

where Δ_{ZPL} is the energy difference between the two state's minima or corresponding ZPLs, $w_{1,2}$ are the transition rates of each state, ${}^2E(G)$ and ${}^4T_1(P)$, respectively. As we will see later on, the most relevant nonradiative deexcitation occurs through the crossover between the ${}^2E(G)$ and the low-lying ${}^4T_1(F)$ excited states, the activation energy of this process being Δ_{act} as it is indicated in the single-mode configurational curves of Fig. 5.

The $\tau(T)$ data of Fig. 4 can be explained with this model. The analysis is divided into two temperature regions for obtaining accurate fit parameters depending on whether the radiative process involving thermal population changes of the ${}^2E(G)$ - ${}^4T_1(P)$ emitting states is the main deexcitation process ($w_1^{nr} = 0$) or whether the nonradiative process becomes dominant. The curves of Fig. 4 and the corresponding fit parameters are least-square fits of $\tau(T)$ data to Eq. (3) following this procedure. The excited-state dynamics is fairly well described with the proposed model and Δ_{ZPL} and Δ_{act} are both consistent with the absorption and PL spectra shown in Figs. 2 and 3 and the configurational energy curves deduced from spectral data (Fig. 5).

C. Pressure study

1. Pressure dependence

The question is whether squeezing MgAl₂O₄:Co²⁺ by external hydrostatic pressure is able to further separate the

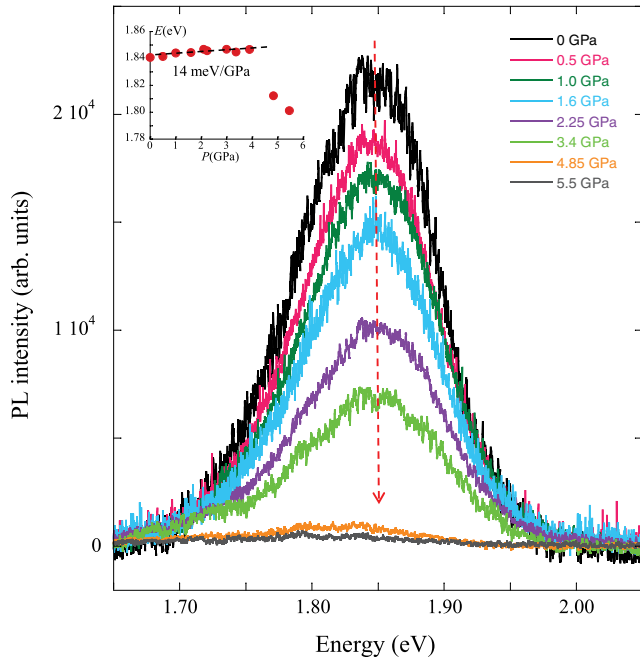


FIG. 6. (Color online) Variation of the time-resolved emission spectrum of $\text{MgAl}_2\text{O}_4:\text{Co}^{2+}$ with pressure at room temperature. Each spectrum was taken 30 ns after the excitation pulse at 530 nm using a counting gate of 10 μs . Note the PL quenching above 5 GPa. The inset shows the variation of the peak energy with pressure as $E(P) = 1.84 + 0.014 P$ (E and P are given in eV and GPa units, respectively).

${}^2E(G)-{}^4T_1(P)$ states in order to enhance the narrow PL from ${}^2E(G)$ at ambient conditions, with an eventual PL quantum-yield increase. This situation is equivalent to what has been observed along the excited-state crossover between the ${}^2E(G)$ and ${}^4T_2(F)$ states in six-coordinated $\text{Cr}^{3+}(O_h)$ in Al_2O_3 (Ref. 20) or LiCaAlF_6 (Ref. 21), involving the ${}^2E(G)$ and ${}^4T_1(P)$ states in the four-coordinated $\text{Co}^{2+}(T_d)$. In either case application of pressure (or likewise increasing Δ/B) enlarges the energy separation between ${}^2E(G)$ and ${}^4T_2(F)$ for Cr^{3+} , or ${}^4T_1(P)$ for Co^{2+} , yielding stabilization of ${}^2E(G)$ as the low-lying emitting excited state.

Figure 6 shows the time-resolved emission spectra as a function of pressure. The corresponding $\tau(P)$ variation is shown in Fig. 7. Upon increasing pressure, we observe a very slight shift of the emission maximum toward higher energy (inset of Fig. 6). However, the more salient feature is the strong decrease of PL intensity with pressure, the PL disappearing above 6 GPa. An analogous behavior is observed for $\tau(P)$. It must be mentioned that the excitation spectra do not change appreciably in this pressure range, thus indicating that the PL quenching must be ascribed to excited-state dynamics rather than to deep changes of electronic structure.

Contrary to expectations, pressure does not enhance the PL quantum yield in Co^{2+} but favors PL quenching. At variance with Cr^{3+} , where pressure yields a PL increase, the effect of pressure in $\text{Co}^{2+}(T_d)$ systems is rather different due to the presence of intermediate excited states.

According to the PL quenching induced at high temperature, here we propose that pressure mainly reduces the

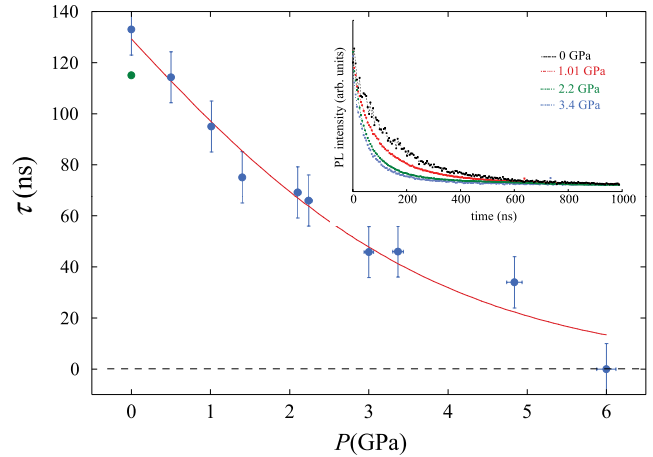


FIG. 7. (Color online) Variation of the room temperature PL lifetime of the emission at 1.84 eV of $\text{MgAl}_2\text{O}_4:\text{Co}^{2+}$ with pressure measured upon pulsed excitation at 530 nm. The inset shows the time-dependent PL intensity at selected pressures. The solid line represents least-square fit to Eq. (4) with the following fitting parameters: $w_1 = (0.33 \pm 0.01) \times 10^6 \text{ s}^{-1}$; $w_2 = (6.5 \pm 1.4) \times 10^6 \text{ s}^{-1}$; $\Delta_{\text{ZPL}} = (27 \pm 2) \text{ meV}$; $w_1^{\text{nr}} = (2.25 \pm 0.16) \times 10^{10} \text{ s}^{-1}$; $\Delta_{\text{act}}^0 = (200 \pm 8) \text{ meV}$; and $\alpha = (11.9 \pm 1.2) \text{ meV/GPa}$ (see text for details).

activation energy for nonradiative processes, thus favoring PL quenching. Although pressure slightly increases the energy separation between ${}^2E(G)$ and ${}^4T_1(P)$ states, initially favoring PL, it also increases the energy of the ${}^4T_2(F)$ state. Furthermore this increase of energy must be also accompanied by a displacement of the state minima due to the strong electron-lattice coupling for ${}^4T_1(F)$ and ${}^4T_2(F)$, as it is schematically shown in Fig. 5. The configurational energy parabola represent states involved in the emission processes, at ambient pressure (solid lines) and high pressure (dashed lines). The pressure-induced shifts indicate that the ${}^2E(G)-{}^4T_1(F)$ crossing point, which is responsible for nonradiative deexcitation through the cascade ${}^2E(G) \rightarrow {}^4T_1(F) \rightarrow {}^4T_2(F) \rightarrow {}^4A_2(F)$, approaches the ${}^2E(G)$ minimum, thus reducing the activation energy Δ_{act} .

Under ambient conditions, the nonradiative activation energy is according to the $\tau(T)$ variation, $\Delta_{\text{act}} = 200 \text{ meV}$, which is high enough to relatively minimize the PL loss at room temperature ($\eta \approx 60\%$). However, the PL loss can increase with pressure if Δ_{act} decreases. The pressure evolution of the lifetime confirms it.

2. Excited-state crossover: Dynamical model

As discussed previously, the lifetime evolution can be described taking into account radiative and nonradiative processes occurring through the ${}^2E(G)-{}^4T_1(F)$ crossover point following Eq. (3). Accordingly, pressure and temperature dependencies of the lifetime have been analyzed considering that the activation energy depends linearly on pressure as $\Delta_{\text{act}} = \Delta_{\text{act}}^0 - \alpha P$, but keeping fixed the other fit parameters. Therefore we fit the data to the following equation:

$$\tau(T, P) = \frac{1 + 3e^{-\frac{\Delta_{\text{ZPL}}}{kT}}}{w_1 + w_1^{\text{nr}}e^{-\frac{\Delta_{\text{act}}^0 - \alpha P}{kT}} + 3w_2e^{-\frac{\Delta_{\text{ZPL}}}{kT}}}. \quad (4)$$

Figures 4 and 7 show the least-square fit using the following parameters for both temperature and pressure dependencies: $w_1 = (0.33 \pm 0.01) \times 10^6 \text{ s}^{-1}$; $w_2 = (6.5 \pm 1.4) \times 10^6 \text{ s}^{-1}$; $\Delta_{\text{ZPL}} = (27 \pm 2) \text{ meV}$; $w_1^{\text{nr}} = (2.25 \pm 0.16) \times 10^{10} \text{ s}^{-1}$; $\Delta_{\text{act}}^0 = (200 \pm 8) \text{ meV}$; and $\alpha = (11.9 \pm 1.2) \text{ meV/GPa}$. It must be pointed out that Δ_{ZPL} was kept constant with pressure. For temperatures above room temperature, this approximation is fairly good since the PL lifetime is mainly governed by nonradiative processes. In fact, if we assume that Δ_{ZPL} increases with pressure, as the emission band, at 14 meV/GPa (inset of Fig. 6), then we obtain the same fitting parameters for the transition rates with the exception of parameter $\alpha = (8.6 \pm 1.0) \text{ meV/GPa}$ that decreases a 20% to consistently compensate the increase of Δ_{ZPL} with pressure when including $\Delta_{\text{ZPL}} = 27 + 14 P$ in Eq. (4).

This result is noteworthy for understanding the visible PL of Co^{2+} in T_d symmetry with the site volume. Opposite to what is commonly accepted, four-coordinated Co^{2+} PL is favored upon tetrahedral volume expansion; i.e., volume contraction yields activation of nonradiative processes. This conclusion is important to understand the optical properties of Co^{2+} in many oxides of interest in optoelectronics ($\text{MgAl}_2\text{O}_4:\text{Co}^{2+}$; $\text{ZnO}:\text{Co}^{2+}$), pigments (CoAl_2O_4), or phosphors ($\text{ZnAl}_2\text{O}_4:\text{Co}^{2+}$; $\text{MgAl}_2\text{O}_4:\text{Co}^{2+}$). Eventually this result may explain some tricky PL behaviors attained in Co^{2+} oxide-based nanoparticles, thin films, or strained structures as due to slight structure modifications induced in such conformations.

IV. CONCLUSIONS

We have demonstrated that Co^{2+} PL in $\text{MgAl}_2\text{O}_4:\text{Co}^{2+}$ originates from the long-lived ${}^2E(G)$ state ($\tau = 3.0 \mu\text{s}$) at low temperature giving rise to a narrow peak structure with

vibrational replicas of 26 meV (210 cm^{-1}). We show that there is an ESCO [${}^4T_1(P) \leftrightarrow {}^2E(G)$] at ambient pressure, which is responsible for the evolution of the emission spectrum from a broadband emission between 300 K and 100 K to a narrow peak emission at 6 K. The PL lifetime decreases exponentially with temperature due to two additional mechanisms: (i) the thermal population of the short-lived ${}^4T_1(P)$ emitting state and (ii) the activation of nonradiative deexcitation channels associated with the ${}^4T_1(F) \leftrightarrow {}^2E(G)$ crossing. The latter mechanism is responsible for the PL quenching observed either above 300 K at ambient pressure ($\Delta_{\text{act}} = 200 \text{ meV}$) or above 6 GPa at 295 K ($\Delta_{\text{act}} < 140 \text{ meV}$).

It has been well established that, instead of enhancing ESCO phenomena, pressure (or volume compression) reduces Co^{2+} PL at tetrahedral sites and eventually suppresses it (PL quenching). This conclusion is opposite to what is generally accepted for PL impurity systems, stating that the lower the transition-metal site volume, the more enhanced the PL. Four-coordinated Co^{2+} systems like those attained in $\text{ZnAl}_2\text{O}_4:\text{Co}^{2+}$, $\text{MgAl}_2\text{O}_4:\text{Co}^{2+}$, or $\text{ZnO}:\text{Co}^{2+}$ behave oppositely and thus PL is favored upon volume expansion. This conclusion is important for understanding and eventually determining the structural requirements for highly efficient PL materials based on $\text{Co}^{2+}(T_d)$ systems.

ACKNOWLEDGMENTS

Financial support from the Spanish Ministerio de Economía y Competitividad (Project No. MAT2011-28868-C02-01) and MALTA INGENIO-CONSOLIDER 2010 (Ref. CDS2007-0045) is acknowledged. L.N. thanks the University of Cantabria for a postdoctoral fellowship grant.

*Present address: Synchrotron SOLEIL, L'Orme des Merisiers, Saint-Aubin BP48, 91192 Gif-Sur-Yvette, France.

†Corresponding author: fernando.rodriguez@unican.es

¹N. V. Kuleshov, V. P. Mikhailov, V. G. Scherbitsky, P. V. Prokoshin, and K. V. Yumashev, *J. Lumin.* **55**, 265 (1993).

²K. V. Yumasev, *Appl. Opt.* **38**, 6343 (1999).

³G. Karlsson, V. Pasiskevicius, F. Laurell, J. A. Tellefsen, B. Denker, B. I. Galagan, V. V. Osiko, and S. Sverchkov, *Appl. Opt.* **39**, 6188 (2000).

⁴V. P. Mikhailov *et al.*, *Digest of Advanced Solid-State Lasers, OSA Technical Digest* (Optical Society of America, Washington, D.C., 1999), pp. 145–147.

⁵X. L. Duan, D. R. Yuan, X. F. Cheng, Z. M. Wang, Z. H. Sun, C. N. Luan, D. Xu, and M. K. Lv, *Opt. Mater.* **25**, 65 (2004).

⁶J. Ferguson, D. L. Wood, and L. G. Van Uitert, *J. Chem. Phys.* **51**, 2904 (1969).

⁷D. R. Stephens and H. G. Drickamer, *J. Chem. Phys.* **35**, 429 (1961).

⁸H. G. Drickamer and C. W. Frank, *Electronic Structure, Electronic Transitions and the High Pressure Chemistry and Physics of Solids* (Chapman & Hall, London, 1973).

⁹R. Burns, *Mineralogical Applications of Crystal Field Theory*, (Cambridge University Press, Cambridge, UK, 1993).

¹⁰D. Rangappa, T. Naka, A. Kondo, M. Ishii, T. Kobayashi, and T. Adshiri, *J. Am. Chem. Soc.* **129**, 11061 (2007).

¹¹P. Koidl, *Phys. Rev. B* **15**, 2493 (1977).

¹²T. P. J. Han, M. Villegas, M. Peiteado, A. C. Caballero, F. Rodríguez, and F. Jaque, *Chem. Phys. Lett.* **488**, 173 (2010).

¹³Ü. Özgür, Ya. I. Alivov, C. Liu, A. Teke, M. A. M. A. Reshchikov, S. Doğan, V. Avrutin, S.-J. Cho, and H. Morkoç, *J. Appl. Phys.* **98**, 041301 (2005).

¹⁴X. Duan, D. Yuan, X. Cheng, Z. Sun, H. Sun, D. Xu, and M. Lv, *J. Phys. Chem. Solids* **64**, 1021(2003).

¹⁵Y. V. Klyucharov and S. A. Suvorov, *Inorg. Mater.* **1**, 1281 (1965).

¹⁶P. J. Dereñ, W. Streck, U. Oetliker, and H. U. Güdel, *Phys. Status Solidi B* **182**, 241 (1994).

¹⁷L. Nataf, F. Rodríguez, R. Valiente, and V. Ulanov, *J. Lumin.* **129**, 1602 (2009).

¹⁸S. Sugano, Y. Tanabe, and H. Kamimura, *Multiplets of Transition-Metal Ions in Crystals* (Academic Press, New York, 1970).

¹⁹D. S. Kenny and A. Navrotsky, *J. Inorg. Nucl. Chem.* **34**, 2115 (1972).

²⁰K. Syassen, *High Pressure Res.* **28**, 75 (2008).

- ²¹M. N. Sanz-Ortiz, F. Rodríguez, I. Hernández, R. Valiente, and S. Kück, *Phys. Rev. B* **81**, 045114 (2010).
- ²²T.-L. Phan, M.-H. Phan, and S.-C. Yu, *Phys. Status Solidi B* **241**, 434 (2004).
- ²³P. J. Derén, M. Malinowski, and W. Strek, *J. Lumin.* **68**, 91 (1996).
- ²⁴R. A. Forman, G. J. Piermarini, J. D. Barnett, and S. Block, *Science* **176**, 284 (1972).
- ²⁵M. B. Kruger, J. H. Nguyen, W. Caldwell, and R. Jeanloz, *Phys. Rev. B* **56**, 1 (1997).
- ²⁶A. B. P. Lever, *Inorganic Electronic Spectroscopy: Studies in Physical and Theoretical Chemistry* (Elsevier, New York, 1984).
- ²⁷Y. Rodríguez-Lazcano, L. Nataf, and F. Rodríguez, *Phys. Rev. B* **80**, 085115 (2009).
- ²⁸X. L. Duan, D. R. Yuan, X. F. Cheng, Z. M. Wang, Z. H. Sun, C. N. Luan, D. Xu, and M. K. Lv, *Opt. Mater.* **25**, 65 (2004).
- ²⁹K. V. Yumashev, I. A. Denisov, N. N. Posnov, P. V. Prokoshin, and V. P. Mikhailov, *Appl. Phys. B* **70**, 179 (2000).
- ³⁰A. M. Malyarevich, I. A. Denisov, K. V. Yumashev, O. S. Dymshits, and A. A. Zhilin, *J. Opt. Soc. Am. B* **19**, 1815 (2002).
- ³¹P. Thibaudeau, A. Debernardi, V. Ta Phuoc, S. da Rocha, and F. Gervais, *Phys. Rev. B* **73**, 064305 (2006).
- ³²I. Hernández, F. Rodríguez, and A. Tressaud, *Inorg. Chem.* **47**, 10288 (2008).
- ³³M. Voda, J. García Solé, F. Jaque, I. Vergara, A. Kaminskii, B. Mill, and A. Butashin, *Phys. Rev. B* **49**, 3755 (1994).
- ³⁴R. Martín-Rodríguez, R. Valiente, F. Rodríguez, and M. Bettinelli, *Nanotechnology* **22**, 265707 (2011).